UCSF

Title

Organic Matrix Derived from Host—Microbe Interplay Contributes to Pathological Renal Biomineralization

Permalink

https://escholarship.org/uc/item/2m9881b9

Journal

ACS Nanoscience Au, 3(4)

ISSN

2694-2496

Authors

Bai, Yushi

Wang, Yongmei

Kang, Misun

et al.

Publication Date

2023-08-16

DOI

10.1021/acsnanoscienceau.2c00060

Peer reviewed

Article

Organic Matrix Derived from Host−Microbe Interplay Contributes to Pathological Renal Biomineralization

Yushi Bai, Yongmei Wang, Misun Kang, Claire M. Gabe, Sudarshan Srirangapatanam, Austin Edwards, Marshall Stoller, Stefan J. Green, Shaul Aloni, Nobumichi Tamura, Elia Beniash, Markus Hardt, and Sunita P. Ho*

Cite This: https://doi.org/10.1021/acsnanoscienceau.2c00060

Read Online

ACCESS | Metrics & More | Article Recommendations | SI Supporting Information

ABSTRACT: Matrix stones are a rare form of kidney stones. They feature a high percentage of hydrogel-like organic matter, and their formation is closely associated with urinary tract infections. Herein, comprehensive materials and biochemical approaches were taken to map the organic−inorganic interface and gather insights into the host−microbe interplay in pathological renal biomineralization. Surgically extracted soft and slimy matrix stones were examined using micro-X-ray computed tomography and various micro-spectroscopy techniques. Higher-mineral-density laminae were positive for calcium-bound Alizarin red. Lower-mineral-density laminae revealed periodic acid-Schiff-positive organic filamentous networks of varied thickness. These organic filamentous networks, which featured a high polysaccharide content, were enriched with zinc, carbon, and sulfur elements. Neutrophil extracellular traps (NETs) along with immune response-related proteins, including calprotectin, myeloperoxidase, CD63, and CD86, also were identified in the filamentous networks. Expressions of NETs and upregulation of polysaccharide-rich mucin secretion are proposed as a part of the host immune defense to "trap" pathogens. These host−microbe derived organic matrices can facilitate heterogeneous nucleation and precipitation of inorganic particulates, resulting in macroscale aggregates known as "matrix stones". These insights into the plausible aggregation of constituents through host−microbe interplay underscore the unique "double-edged sword" effect of the host immune response to pathogens and the resulting renal biominerals.

KEYWORDS: pathological biomineralization, kidney stone, matrix stone, urinary tract infection, immune response, organic filamentous networks
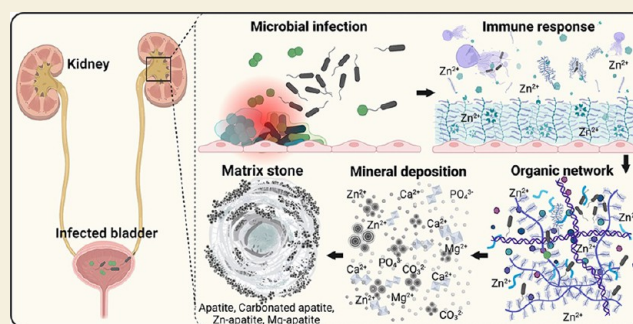
INTRODUCTION

Biofilms are well-organized microbial communities that form on inanimate or living surfaces.[1] Within a biofilm, microbes are embedded in the self-produced extracellular polymeric matrix that provides resistance against antimicrobial agents and host immune defense.[2] Urinary tract infections (UTIs) and associated biofilm complications affect 150 million people each year worldwide.[3] Uropathogen biofilms adhering to uroepithelium are often responsible for persistent and recurrent infections and can cause pyelonephritis and acute prostatitis.[4,5] Uropathogen virulence determinants include surface factors, such as fimbriae, adhesins, and pili, and extracellular factors, such as toxins, siderophores, enzymes, and polysaccharide coatings. These factors are critical for breaching the host mucosal barrier and subsequently result in colonization on uroepithelium to establish an infection.[3,4] At the host−microbe interface, the extracellular polymeric substances (EPSs) of the biofilm can be very complex: in addition to microbe-secreted exopolysaccharides and extra-

cellular DNA, host-derived proteins, mucopolysaccharides, and nucleic acids, whole host cells may also be present.[6−8]

An extended complication of biofilm is its mineralization and subsequent calculi formation[5,9,10] which is not unique to the kidney but also occurs in the mouth as subgingival calculus.[11,12] Both the bacterial cell surface and EPS play collective roles in attracting ions and subsequent precipitation of minerals. Specifically, carboxylic and phosphate anion groups on microbial cell surfaces can provide a net negative charge that can sequester various cations including Ca^{2+}, Mg^{2+}, Na^+, and Zn^{2+} from the surrounding milieu. Additionally, polysaccharides with varied length and composition,[13] nucleic

A

acids, and proteins in the EPS also contain carboxyl, phosphate, amine, and hydroxyl groups that have a high binding affinity for these commonly identified cations.[14,15] Four plausible mechanisms for bacteria-induced mineralization that could result in urinary stone formation have been proposed. These include (1) bacterial adherence to a pre-existing mineral; (2) bacterial citrate lyase production can result in a decrease in urine citrate levels; and (3) bacteria—crystal aggregates may bind with the renal tubular epithelium and induce matrix protein secretion that can act as nucleators/precursors for mineral formation.[16,17] The more commonly discussed mechanism is that (4) unique ureolytic bacteria can hydrolyze urea to ammonium ions, which increases the local pH and facilitates the formation of magnesium (Mg)- and ammonia (NH_3)-based struvite and carbonate-(CO_3) based apatite crystals.[10] In the physiological context of a patient, the aforementioned mechanisms are likely to coexist and collectively contribute to complex biofilm and associated calculi formations.

Matrix stones are a rare form of calculi among all urinary stones, as they are limitedly identifiable using patient-care X-rays. Matrix stones are soft, radiotransparent, and fragile with lower mineral content, in contrast to the commonly identified hard calcium oxalate and calcium phosphate kidney stones.[18] Female patients with UTI are closely associated with matrix stones[19] that contain a significant amount of fibrous network.[20] This fibrous network presents itself as a powerful platform to investigate the interplay between microbe-constructed biofilm and host immune response-related products and subsequent biomineralization. Most reports on matrix stones are limited to case studies,[20,21] and the physicochemical characteristics needed to gather insights into matrix stone formations are yet to be investigated. Herein, we performed systematic, top-down characterizations from millimeter to micrometer to nanometer length scales on surgically extracted matrix stones to underpin the fact that their formation lies at the interface between microbe activity and host immune response.

■ MATERIALS AND METHODS

Sample Collection and Preparation

Surgically extracted matrix stones from patients following a protocol approved by the UCSF Committee on Human Research Protection Program (IRB # 14-14533) were imaged and analyzed using multiple analytical techniques. Corresponding clinical lab analyses on urine cultures and matrix stone compositions are shown in Table S1.

Fresh matrix stone specimens were snap-frozen and stored at −80 °C for microbe community characterization and proteomics. For all other characterizations, matrix stone specimens were fixed in 10% neutral buffered formalin (Richard-Allan Scientific, Kalamazoo, MI) at 4 °C overnight, washed three times in phosphate-buffered saline, and subsequently washed with distilled water for 30 min. Specimens were stored in 70% ethanol solution at 4 °C for further characterization.

Micro-X-ray Computed Tomography

Specimens ($N = 3$) were scanned in 70% ethanol using micro-X-ray computed tomography (micro-XCT) (MicroXCT-200; Carl Zeiss Microscopy, Pleasanton, CA) at 4× (5 μm/voxel) and 10× magnifications (3 μm/voxel) with 1200 image projections and an angle sweep from −93 to 93°. Specimens were scanned with a source power of 50 and 60 kVp for 4× and 10× magnifications, respectively. Mineral densities (MD) of matrix stone specimens were determined using 4× magnification scans. The reconstructed images of the specimens were analyzed using Avizo 2019.4 software (Fisher

Scientific, Hillsboro, OR). X-ray intensity values were converted from Hounsfield units to MD (mg/cc).[22]

Histology and Microscopy

The fixed specimens ($N = 3$) were embedded in paraffin, and 5 μm thick sections were mounted on glass slides. Mounted sections were stained with H&E, Alizarin red, and periodic acid-Schiff (PAS) to detect the distribution of basophilic and acidophilic regions, calcium deposits, and polysaccharides, respectively. Stained specimen sections were imaged and recorded using an optical microscope (BX-51, Olympus, Waltham, Massachusetts).

Immunohistology

For immunohistochemistry, epitope retrieval on serial sections was achieved with 0.1 M sodium citrate buffer (pH = 6.0) for 30 min at 80 °C for all sections. Blocking was performed on all sections with a commercialized blocking agent (Intercept (TBS) protein-free blocking buffer, LI-COR, Lincoln, Nebraska) at room temperature for 1 h. Primary antibodies, including anti-CD63 (rabbit polyclonal, ab231975, Abcam, Cambridge), anti-CD86 (mouse monoclonal, ab220188, Abcam, Cambridge), anti-myeloperoxidase (rabbit monoclonal, ab208670, Abcam, Cambridge), and anti-calprotectin (mouse monoclonal, ab22506, Abcam, Cambridge) were incubated on the sections under static conditions overnight at 4 °C. The sections were further incubated under static conditions with secondary antibodies at room temperature for 1 h. The secondary antibodies used to visualize CD63 and myeloperoxidase distributions were goat anti-rabbit IgG H&L-Alexa Fluor 555 (ab150078, Abcam, Cambridge), while the secondary antibodies used to visualize CD86 and calprotectin were donkey anti-mouse IgG H&L-Alexa Fluor 488 (ab150105, Abcam, Cambridge) and goat anti-mouse IgG H&L-Alexa Fluor 647 (ab150115, Abcam, Cambridge), respectively. The mounting solution contained DAPI for DNA detection (ab104139, Abcam, Cambridge). Immunolocalization experiments were accompanied by a blank control slide (incubated only in blocking solution) and secondary antibody-only slides (replacing the primary antibody with blocking solution) to assess the level of autofluorescence and non-specific staining. The specimens were routinely examined using an optical microscope with various fluorescence filters (BX-51, Olympus, Waltham, Massachusetts).

Confocal Imaging

CD63, CD86, and DNA localization. Sections of matrix stones were imaged with a Leica SP5 laser scanning confocal system. Lower magnification images were acquired with 20× air objective. Higher magnification images were acquired using a 63.0× (N.A. 1.40) oil objective. For individual channels, imaging was performed with excitation at 488 nm (51% intensity) and acquisition at 500−600 nm with a gain of 882. The same tissue also was imaged using excitation at 405 nm (with 27% intensity) and acquisition at 430−550 nm with a gain of 844.

For image analysis, the Imaris (Bitplane, v9.7.2) "coloc" module was used to find voxels where signal was present in both channels (threshold = 2000 for both channels). A third channel was created using colocalized signals, and surface objects were created (intensity threshold = 17606). The surface objects were filtered by size, and all surfaces with less than 2000 voxels were discarded; the results are shown as a 3D model.

Calprotectin, Myeloperoxidase, and DNA Localization. Matrix stone sections were imaged with a Nikon spinning disk confocal using a 4× air objective and a 60× (N.A. 1.49) oil objective. Imaging at 4× generated a tiled image showing a larger area of the specimen. Z-stacking of images (step size = 0.2 μm) was performed at 60× to investigate structural details. The specimen was excited at 647, 561, and 405 nm sequentially, and respective emissions using a 500 ms exposure were captured accordingly. For image analysis, we used Imaris (Bitplane, v9.7.2) to create surface objects on each channel by setting the intensity threshold to two standard deviations above the mean intensity for each channel. The total volume of each surface group was measured using Imaris for calculating the ratio of each component.

Field Emission Scanning Electron Microscopy

Matrix stone specimens ($N = 6$) were dehydrated using an ascending series of ethanol solutions (from 70 to 100%) and were subsequently desiccated for field emission scanning electron microscopy (FESEM) (SIGMA VP500, Carl Zeiss Microscopy, Pleasanton, CA). Surface morphologies of matrix stones were imaged using electrons at 1 keV.

Transmission Electron Microscopy and Immunogold Labeling

The softer parts of the matrix stone specimens ($N = 6$) were dehydrated using ascending series of ethanol solutions (from 70 to 100%) and subsequently embedded in LR-White resin (Electron Microscopy Sciences, Hatfield, PA). Sections with 70−90 nm thickness were cut with an ultramicrotome (Ultracut E, Reichert-Jung) and mounted on Formvar-coated 200-mesh copper grids (Ted Pella, Redding, CA). To ensure visualization of organic content in matrix stone specimens, some sections on EM grids were demineralized on top of a 1 mM HCl droplet for 5 min and subsequently stained with a droplet of 2% methylamine tungstate (Nano-W, Nanoprobes, Yaphank, NY) for 45 s. Transmission electron microscopy (TEM) imaging was performed on a JEOL JEM-1400 microscope (JEOL USA, Peabody, MA) operating at 120 kV. Data were recorded with a 4k Gatan Ultra Scan CCD camera (Gatan, Pleasanton, CA).

For immunogold labeling, the demineralized sections were incubated in a primary CD63 (rabbit polyclonal, ab231975, Abcam, Cambridge) antibody solution for 6 h at 37 °C. Excessive primary antibody was washed off with DI water; the sections were further incubated in secondary goat anti-rabbit IgG with 10 nm colloidal gold labeling (BosterBio, Pleasanton, CA) for 1 h under room temperature. Excessive antibody was washed away with DI water, and the sections were stained with a droplet of 2% methylamine tungstate (Nano-W, Nanoprobes, Yaphank, NY) for 45 s, wick-dried, and stored for TEM imaging.

Energy-Dispersive X-ray Spectroscopy

The chemical composition of matrix stone specimens was acquired using energy-dispersive X-ray (EDX) spectroscopy (Bruker AXS, Madison, WI) at 10−15 keV. Data acquisition was performed in Esprit 2 software (Bruker Nano Inc., Madison, Wis., US). Principal component analysis on elemental data acquired from the EDX scanner specific to higher and lower zinc (Zn) (HZ, LZ) regions was performed using GraphPad Prism (GraphPad Software, Version 9.5.1, Boston, MA).

Microprobe X-ray Fluorescence Spectroscopy

Elemental maps specific to Zn, in addition to commonly identified calcium (Ca) and phosphorus (P) of matrix stone specimens were collected using microprobe X-ray fluorescence spectrometer (μXRF) at beamline 10.3.2 of the Advanced Light Source at Lawrence Berkeley National Laboratory. Spatial maps of elemental counts were generated using an incident energy beam of 10 KeV and a spot size of $\sim 7 \times 7$ μm. 2D correlative scatter plots of Ca−P, Ca−Zn, and P−Zn were obtained to identify the spatial association of elements using R version 3.6.3 (R Core Team 2020).

Micro-X-ray Diffraction Analysis

Synchrotron 2D micro X-ray diffraction (μ-XRD) patterns were collected at beamline 12.3.2 of the Advanced Light Source, Lawrence Berkeley National Laboratory, with a monochromator set at an energy of 10 keV (wavelength $\lambda = 1.2398$ Å) and using a reflective geometry. The area detector (DECTRIS Pilatus 1M) was placed at an angle of 40° at a distance of 156 mm from the sample surface. The X-ray beam spot was about 10×3 μm. The data were processed through the in-house-developed software XRDSol. Lattice parameters were refined by fitting over 5 reflections.

Fourier Transform Infrared Spectroscopy

Tissue sections mounted on quartz slides were analyzed using a polarized microscope prior to Fourier-transform infrared (FTIR) spectroscopy. Polarized microscopy was performed to identify areas with lower and higher degrees of mineralization. The section was studied using a Lumos II FTIR microscope (Billerica, MA) in the attenuated total reflectance (ATR) mode. The section was studied at 4 cm^{-1} resolution, and 64 spectra were collected per acquisition. The spectra were analyzed with Spectrum 10 spectrum management software (PerkinElmer, Branford, CT) and graphed using the OriginLab Pro software package (OriginLab Corporation, Northampton, MA). ATR spectra were acquired from three distinct regions of the matrix stone section.

Liquid Chromatography Tandem Mass Spectrometry

Three matrix stones were individually mixed with dry ice and pulverized using a ceramic mortar and a marble pestle. 200 mg of the resulting stone powder were incubated in 4 mL of extraction buffer (4 M guanidine HCl, 0.5 M EDTA, 65 mM EDTA, and 50 mM Tris-HCl, pH 7.4) for 48 h at 4 °C after being sonicated three times for 10 s. Insoluble material was subsequently removed by centrifugation at 15,000g at 4 °C for 15 min. Protein extracts were prepared for mass spectrometric analysis using a modified version of the filter-aided sample preparation protocol.[23]

Liquid chromatography−tandem mass spectrometry (LC−MS/MS) in data-dependent acquisition mode was performed on an Easy-nLC 1000 system hyphenated to an Orbitrap Fusion mass spectrometer equipped with an Easy Spray ESI source (Thermo Fisher Scientific, Waltham, MA). Detailed MS-acquisition parameters are described in the Supplemental Methods. Protein identification and label-free quantification were performed using the PEAKS Studio XPro software suite (Bioinformatics Solution). The false discovery rate for peptide identifications was controlled using the decoy-fusion method. FDRs of 1% were applied at the peptide spectrum and protein match level, and only protein hits with two significant peptide identifications were retained for further analysis. For the relative quantitation of proteins, the peak areas of the top 3 most abundant unique peptides were employed. Gene ontological overrepresentation in the matrix stone proteome composition was tested against the Reactome pathway database using PANTHER[24] and the complete human proteome as a reference database while correcting for multiple testing according to Bonferroni. The mass spectrometry-based proteomics data have been deposited to the ProteomeXchange Consortium via the PRIDE repository[25] with the dataset identifier: PXD033298.

16S rRNA Sequencing

An additional $N = 3$ specimens were pulverized, as described above. Genomic DNA was extracted from the pulverized specimens using a QIAamp PowerFecal Pro DNA Kit (Qiagen, Germantown, MD). Briefly, pulverized specimens suspended in DNA/RNA Shield were added to PowerBead tubes containing solution CD1 and homogenized on a TissueLyser II device (Qiagen, Germantown, MD) for 3 cycles of 2 min at 30 Hz, with 1 min at 4 °C in between each cycle. After centrifugation, the supernatant was processed on a QIACube Connect device, implementing the IRT version of the QIAamp PowerFecal Pro DNA protocol. Genomic DNA extracted from matrix stones was used as a template for 16S ribosomal RNA gene amplification and next-generation sequencing using a two-stage PCR protocol, as described previously[26] and employing primers targeting the V4 variable region of microbial 16S rRNA genes.[27] Amplicons were pooled and sequenced on an Illumina MiniSeq sequencer with a mid-output flow cell, employing paired-end 2×154 base reads. Raw sequence data were processed as described previously[27] using the DADA2 pipeline within the QIIME2 software package.[28,29] No reagent contaminants were identified using the decontam package based on the prevalence of amplicon sequence variants (ASVs) in the reagent negative blank controls ($n = 6$ PCR reagent controls and $n = 1$ extract reagent control) using default parameters.[30] Unassigned, eukaryote, chloroplast, and mitochondrial ASVs were removed from datasets prior to statistical analyses. Raw sequence data were deposited in the NCBI Sequence Read Archive under BioProject PRJNA942323. DNA extraction, library preparation, sequencing, and bioinformatics analysis were performed at the Genomics and
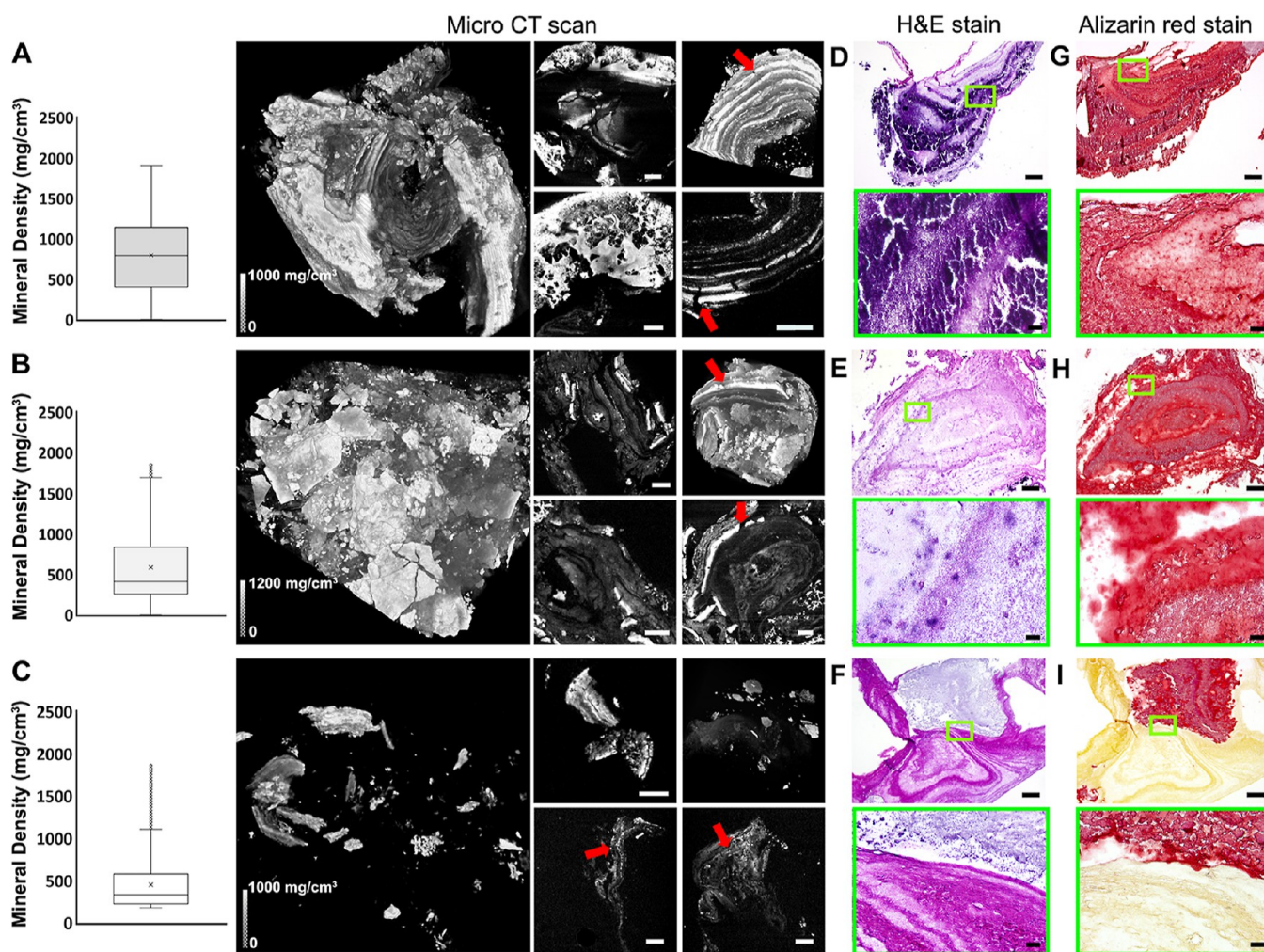
Figure 1. Matrix stones feature laminae with varying mineral densities. (A−C) Matrix stones demonstrate a heterogeneous structure; quantitative analyses revealed diverse mineral densities across specimens. Despite structural heterogeneity, matrix stones exhibited distinctive laminae with lower and higher mineral densities (red arrows), scale bar for micro-CT images: 500 μm. Similar laminae also were observed in (D−F) H&E and (G−I) Alizarin red-stained sections (upper panel scale bar: 200 μm; lower panel scale bar: 20 μm).

Microbiome Core Facility (GMCF) at the Rush University Medical Center.

RESULTS AND DISCUSSION

Matrix Stones Feature Gel-like Organic and Mineralized Laminae

The potential severe aftermath of a relatively "soft" gel-like matrix (Figure S1A−I) growing into a "hard" large staghorn-shaped stone (Figure S1J−K) calls for a deeper understanding of its formation. As such, the physicochemical characteristics of matrix stones that would help provide insights into their etiology are discussed.

The mineral densities (Figure 1A−C) of surgically retrieved matrix stones (Figure S1, Table S1) demonstrated a heterogeneous distribution of mineral densities. X-ray tomograms revealed laminae as a characteristic feature of matrix stones (Figure 1A−C). The layered pattern also was observed in sections stained with H&E (Figure 1D−F) and Alizarin red (Figure 1G−I).

Major Constituents of Matrix Stones Include Minerals, Encrusted Microbial Colonies, and Organic Filamentous Networks

The morphology of a representative matrix stone, consisting of both soft organic and hard inorganic phases (Figure 2A-top, optical image), was analyzed using a scanning electron microscope (SEM) (Figure 2A-bottom, SEM image). In addition to the visually apparent larger mineral pieces (Figure 2A,B), mineral deposits of various sizes and shapes (Figure 2B inserted and Figure 2C) suggested potential growth from numerous nuclei. The soft and slimy portion of the matrix stone contained filamentous networks (Figure 2D). Spherical and rod-like structures, as well as imprints, also were identified within the matrix (Figure 2E,F). Spheres resembled bacteria from the genus *Staphylococcus* with a diameter of 2 ± 0.6 μm (Figure S2A), and rods resembled Gram negative bacteria (Figure S3A, red arrows). A larger size compared to the recognized size of *Staphylococci* of 0.5−1.5 μm[31] could result from mineral precipitation on the cell membrane. Broken spheres with hollow spaces and 20−45 nm thick mineralized wall structures and/or calcium precipitates also were observed (Figure S2).[32] Compared to FESEM, it should be noted that cryoelectron microscopy of the specimens are warranted for an
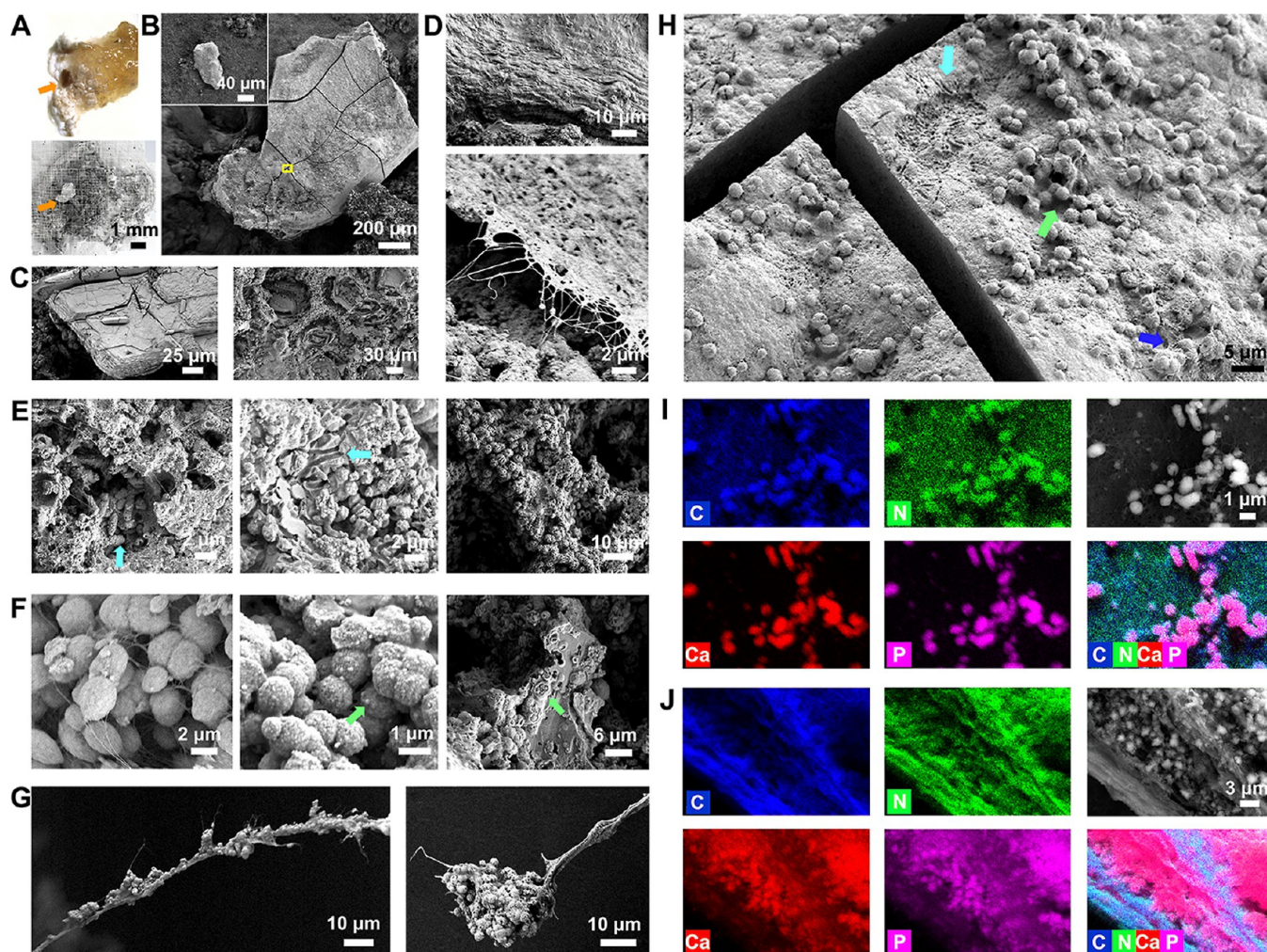
Figure 2. Minerals, encrusted microbial colonies, and organic filamentous networks are major constituents of matrix stones. (A) Optical microscope image (top) and corresponding stitched SEM image (bottom) of a representative matrix stone specimen. (B) Stitched SEM image of the large mineral piece observed in A (indicated with orange arrows); the inserted SEM image shows a smaller mineral deposit. (C) Diverse mineral morphologies were identified within the same specimen. (D) SEM image of the soft, slimy matrix as an extensive film (top) formed from interwoven filamentous networks (bottom) is shown. (E) SEM images of rod-shaped bacteria with grainy surfaces (indicated with a cyan arrow, left panel) and rod-shaped imprints (indicated with a cyan arrow, middle panel) are shown. These embedded bacterial colonies grew into large concretions (right panel). (F) Spherical bacteria (left panel) also developed a grainy appearance (middle panel, mineral deposit on bacterial surface indicated with a green arrow) and grew into large, encrusted aggregates (mineral encrustation indicated with a green arrow). (G) Representative SEM images focused on regions with individual bundles of filaments. These bundles provided scaffolds facilitating heterogeneous nucleation and mineral deposition. (H) High-magnification SEM image of a surface area of a stone piece in B (corresponding area indicated with a yellow box) showed a combination of rod-shaped bacterial imprints (cyan arrows), spherical bacteria (green arrow), and filamentous structures (blue arrow). (I) Elemental analyses demonstrated strong signals representative of organic (carbon and nitrogen) and inorganic (calcium and phosphorus) components, consistent with mineral deposition on bacterial surfaces as observed in E and F. (J) Representative elemental analyses illustrated carbon and nitrogen-rich filaments, while the deposited structures were rich in calcium and phosphorus. These observations demonstrated the organic nature of the filamentous networks, which provided a large surface area for mineral nucleation and precipitation, as seen in G.

accurate representation of the cellular structure of spheres and rods (see identified genera in Figure. S4 and Table S1). Mineral particulates on filaments (Figure 2G) indicate filamentous scaffolds with large surface area can facilitate nucleation. With the filamentous network (Figure 2D) intertwined with other constituents, including microbes and minerals (Figure S3), a stone piece is often presented as a heterogeneous aggregation of all major components (Figure 2H). Aggregates on carbon- and nitrogen-rich microbial cell surfaces (Figure 2I) and filaments (Figure 2J) were positive for calcium and phosphorus. These observations indicated that both the microbial cell surface and filaments are organic constructs serving as substrates for heterogeneous nucleation

and mineral deposition. The organic (Figure 3) and inorganic phases within matrix stones, and their elemental heterogeneity were further characterized and are highlighted through elemental analyses (Figures 4 and 5).

Host Immune Response Contributes Significantly to the Formation of the Organic Filamentous Network

Sections from matrix stones were immunolocalized for CD63, CD86, and nucleic acids (DNA) (Figures 3A and S4). The immunofluorescent laminae (Figure 3A) were strikingly similar to the laminae revealed by varied X-ray attenuation, H&E, and Alizarin red stains (Figure 1). The prevalence of CD63 and CD86 indicated exosomes[33,34] provided insights into question of whether their presence resulted from immune cells.[35−37]
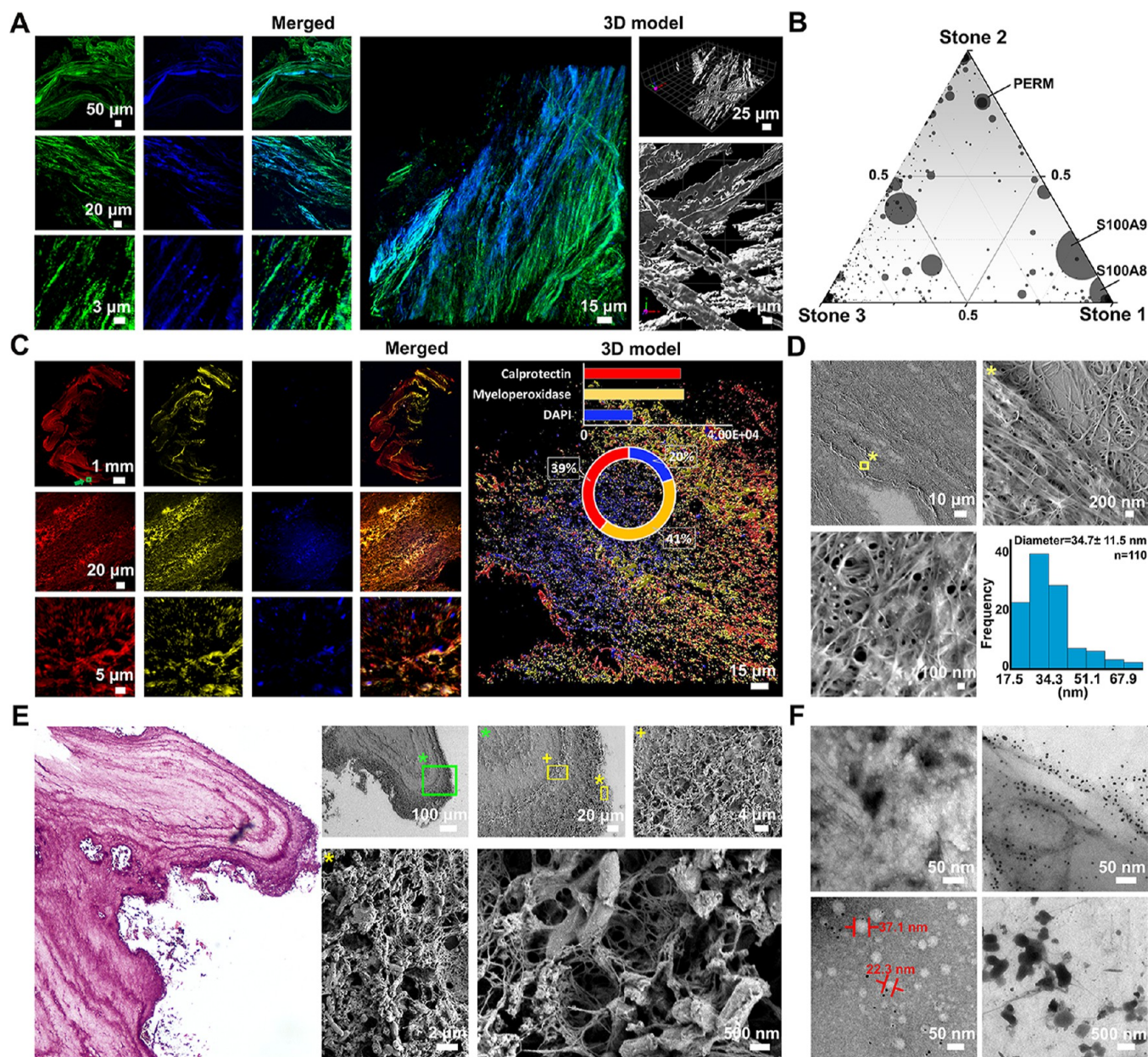
Figure 3. Host immune response and organic filamentous network. (A) Matrix stone stained positive for CD86 (green-left column) and DAPI (blue-middle column), demonstrating the presence of filamentous DNA structures. Z-stacks of optical sections obtained using confocal microscopy showed three-dimensional laminae of the filamentous network. (B) Relative protein composition of the three matrix stones was compared using LC−MS/MS-based proteomics. The ternary plot depicts the average protein abundance (circle size) and the relative ratio of proteins across stones. Functional enrichment analyses revealed an overrepresentation of innate immune factors such as S100A8/A9 (calprotectin) and myeloperoxidase (PERM) associated with NET formation (Table S2). (C) Confocal fluorescence images of matrix stone specimens illustrated distributions of calprotectin (red-left column), myeloperoxidase (yellow-middle column), and DNA molecules (blue-right column) at various magnifications. A 3D model was generated with masks with signals above mean + 2*standard deviation intensities in individual channels. The sum volume from each channel generated a percentage of calprotectin/myeloperoxidase/DNA as 39%:41%:20%. (D) Correlative SEM images of the fluorescence-labeled specimen in C (corresponding area indicated as a green box) revealed the filamentous networks. Higher magnification images demonstrated the coexistence of laminae and spheres with diameters of 34.7 ± 11.5 nm, $n = 110$. (E) PAS-stained sections revealed a similar banding pattern. Correlative microscopy with increasing magnifications using SEM revealed extensive filamentous networks and local thickening, resulting in a lamina; higher magnification images highlighted rod-shaped bacteria trapped in filamentous networks. (F) TEM images revealed filaments and 20−40 nm diameter spheres. Bacteria with long flagella also were identified within the organic matrix.

CD86, in addition, plays a crucial role in the initiation and maintenance of an immune response.[38] It is often used as a M1 macrophage marker but also is contained in secretory vesicles and neutrophil granules.[39,40] DAPI stain indicated DNA structures, which are released as critical components of neutrophil extracellular traps (NETs) during acute inflamma-tion.[41−43] Z-stacking of optical slices of the matrix stone sections revealed a three-dimensional laminar architecture of the network (Figure 3A right panel). Strong signals of these organic molecules through the Z-stack suggested a significant contribution from the host immune system.
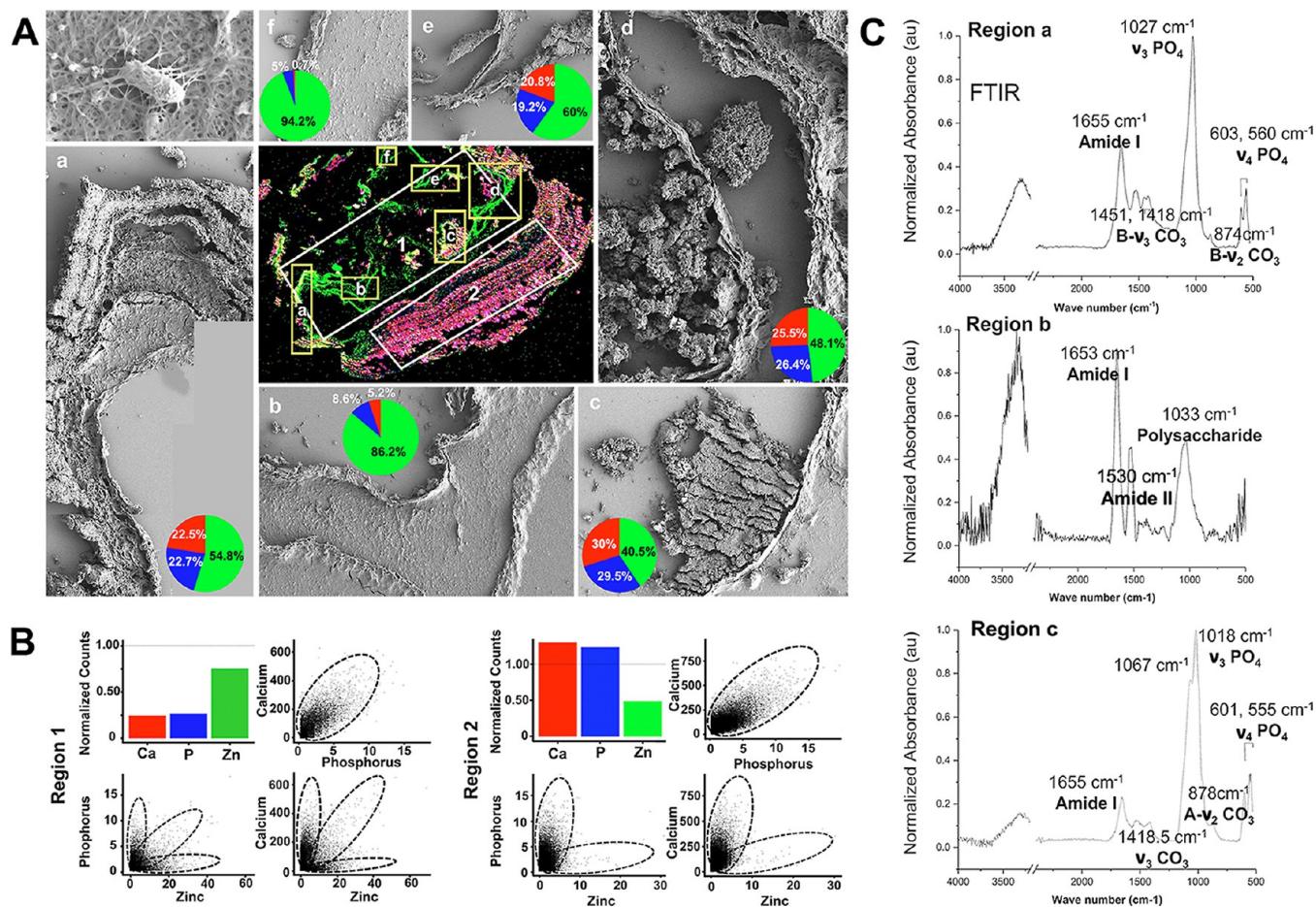
Figure 4. Zinc dominated organic regions contain polysaccharides and amides, and calcium dominated regions contain Zn, Mg, and CO_3 incorporated apatite. (A) XRF analysis of a representative matrix stone section illustrates the distribution of calcium (red), phosphorus (blue), and zinc (green) elements. The map is further divided into zinc-rich (region 1) and calcium/phosphorus-rich (region 2) areas. Additional microenvironments are labeled a-f, and their Zn, Ca, and P ratios are shown as pie charts. SEM images of a-f illustrate the morphological differences of areas with various levels of mineralization. An additional SEM image (top left) illustrates bacteria entrapped in a filamentous network rich in zinc. (B) Quantitative analysis of regions 1 and 2 measured Zn/Ca/P ratios as 59.5%:19.4%:21.1% and 16.2%:43.0%:40.8%, respectively. Scatter plots show correlations between Ca/P, P/Zn, and Ca/Zn. (C) FTIR spectra for regions a−c.

To further confirm immune reactions to pathogens and to provide a comprehensive list of proteins in matrix stones, LC−MS/MS-based proteomics was performed and identified over 747 proteins across stone specimens (Table S2), ranging in abundance over 6 orders of magnitude (Figure S5A). Overall compositional comparison of the matrix stone proteomes revealed similarities between individual matrix stones as well as inter-stone variability (Figure 3B). Specifically, functional enrichment analysis detected a significant overrepresentation of pathway components of the innate immune system and neutrophil degranulation and NET formation (Table S3, Figure S5B,C).[44] Among these proteins, the most abundant were S100A8 and A9 (which complex to form calprotectin), myeloperoxidase, and azurocidin, all of which are proteins contained in neutrophil granules and are involved in the antimicrobial activities of the NETs.[45−48] Calprotectin and myeloperoxidase were selected for immunolocalization and revealed wide signal distribution throughout the laminae (Figure 3C).

SEM images of a representative area (indicated with a green box in Figure 3C, top left panel) on immunolabeled specimens revealed extensive filamentous networks (Figure 3D). Local bands with enhanced immunolabeling signals were associated with thick regions of the network (Figure 3D, top row). Higher magnification confocal (Figure 3A,C, bottom row) and SEM images (Figure 3D, bottom row) also illustrated spheres (diameter of 34.7 ± 11.5 nm, $n = 110$) within networks.

Notably, in Figure 3A,C, volumes of DAPI-positive DNA molecules were less than those from CD86, calprotectin, and myeloperoxidase positive regions. Further quantifications were achieved by segmenting structures with strong fluorescence signals from the 3D volume reconstructed by stacking optical sections positive for DNA, calprotectin, and myeloperoxidase. Fluorescence intensities above the mean value + 2 × standard deviation for each channel were used to eliminate the influence of background, and the percentage of calprotectin/myeloperoxidase/DNA was 39%:41%:20%. The smaller volume for the DNA scaffolds is an interesting finding, as extracellular DNA is traditionally recognized as the major contributor to the filamentous scaffolds in NETs.[42,49] Taken together, we hypothesize that the presence of vesicles and filaments in matrix stone extends beyond NETosis and that other host−pathogen related mechanisms also could contribute to the network formation.

The mucosa of the urinary tract provides a protective barrier from microbes and is a critical component of host immune
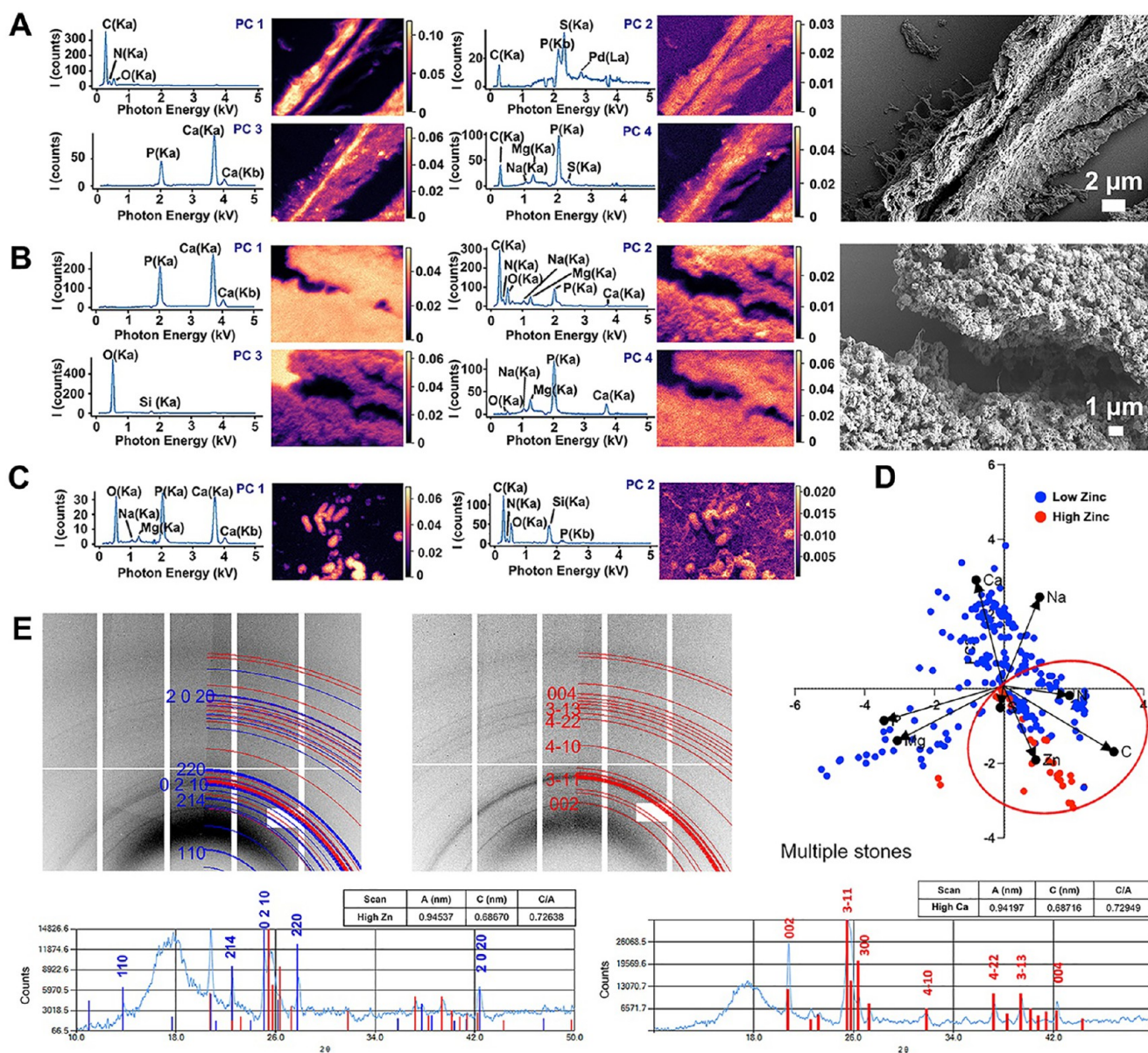
Figure 5. Energy dispersive X-ray spectroscopy of matrix stones and principal component analyses illustrate transformation of organic into an inorganic matter. X-ray diffraction illustrate Zn incorporation in HA. EDX scans and spectra, and PCA analyses of elemental counts for (A) Zn-rich region with thick filamentous networks, (B) highly mineralized area, and (C) encrusted microbial colonies. Note: Pd-palladium signal originates from the specimen coating for SEM. (D) PCA analysis of multiple matrix stones demonstrates Zn, C, S, and N in higher zinc regions (red circle) and Ca, Na, P, and Mg in lower zinc regions. (E) XRD analyses of both high-Zn (left) and high-Ca (right) regions.

defense. The expression of gel-forming mucins can be upregulated by inflammatory factors.[50] In this study, rod-shaped *Proteus mirabilis* and associated proteins were identified to different extents (Table S4). In addition, genera of pathogens including *Staphylococcus*, *Pseudomonas*, *Proteus*, and *Veillionella*, among others, were also identified (Figure S6 and Table S1). Neutrophils in a battle against these pathogens can stimulate increased mucin production and secretion via elastase release.[51,52] With characterized neutrophil activities (Figure 3B,C) in addition to the gel-like appearance of matrix stones (Figures S1 and 2), it is conceivable that mucins secreted by renal epithelial cells are also important components of the stone substrate. Supporting our hypothesis, matrix stone sections stained positive with PAS, indicating abundant polysaccharides as the other organic

constituent (Figures 3E and S7). At a larger scale, these networks also contained local "pockets" with entrapped microbes, a plausible defense against infection progression (Figures 3E and S7).[52]

TEM imaging of anti-CD86 gold labels further confirmed host immune defense-derived filaments and the 20−40 nm spherical structures as critical constituents of matrix stones (Figures 3F and S5). Flagella-like filaments also were observed (Figure 3F, right bottom corner).

Presented comprehensive physicochemical and biochemical analyses provided insights into host immune responses, especially NETosis and mucin secretions, both of which play significant roles in the formation of the organic filamentous networks and subsequent mineral precipitation. These processes that represent host efforts to protect from bacterial

infections but conversely contribute to stone formation, reveal a unique "double-edged sword effect" of the host immune response to microbial attack.[53]

Trace Elements Play Critical Roles in Mineral Formation

The significance of Zn as an immune regulator was noted through the increased risk for infections in humans with zinc deficiency.[54,55] Neutrophil granulocytes, as one type of polymorphonuclear leukocytes, are the first line of defense against invading microbes. The battle between neutrophils and microbes results in a rise of reactive oxygen species, DNA, chromatin, and granule proteins, such as S100A8 and A9 (which form the calprotectin complex), myeloperoxidase, and azurocidin, in the extracellular space.[56] These fundamental constituents of NETs are noted to be Zn positive.[57] Consequently, NETs that capture microbes and contribute to matrix stone formation should also exhibit Zn-positive characteristics.

Spatial heterogeneities of Zn in matrix stones were mapped using XRF, FTIR, EDX, and XRD techniques. Zn-positive regions revealed via XRF were categorized as higher-Zn (region 1 in composite image > median counts) and lower-Zn regions (region 2 in composite image < median counts) (Figures S8 and 4A). Regions 1 and 2 featured Zn/Ca/P ratios of 60%:19%:21% and 16%:43%:41%, respectively (Figure 4B). Ca and P exhibited a strong positive linear correlation in both regions. However, scatter plots of Zn/Ca and Zn/P in each region showed a complex pattern with various clusters (Figure 4B). Patterns included: (1) higher Zn counts with lower Ca or P counts, indicative of organic matrices with lower calcium phosphate mineralization levels (no discernible XRD); (2) higher Zn and Ca/P counts, indicating greater mineralization levels following the scaffold of an organic substrate; (3) lower Zn but higher Ca/P counts, suggesting calcium phosphate mineral precipitation with little to no organic substrate association.

Additional representative microenvironments with varied mineralization levels were labeled as regions a–f. Corresponding SEM images revealed organic networks and laminae as zinc-rich regions. In contrast, the morphology of calcium- and phosphorus-rich regions exhibited a coarse and rigid appearance (Figure 4A).

FTIR and polarized light microscopy characterizations were conducted on representative regions a–c for detailed compositional analysis. Polarized microscopy (Figure S9) revealed birefringent regions a and c (Figure 4A), suggesting a higher degree of mineralization. In contrast, polarized microscopy confirmed the lack of minerals in the zinc-rich region b. FTIR spectra from this nonmineralized area revealed that proteins are the major component based on the strong Amide I (1653 cm^{-1}) and Amide II (1530 cm^{-1}) peaks (Figure 4C, region b). We ruled out the possibility that the peak at 1033 cm^{-1} is ν_3 PO$_4$ since this spectrum lacked characteristic ν_4 PO$_4$ peaks,[58,59] which featured prominently in two other spectra from more mineralized regions. We therefore assigned this peak to polysaccharides, which absorb strongly in the 1200−1000 cm^{-1} region.[60]

The mineral in regions a and c was identified as hydroxyl-deficient carbonated apatite. In region a, a very strong peak with a maximum at ∼1020 cm^{-1} corresponding to ν_3 PO$_4$ and a double peak with maxima at ∼603 and 560 cm^{-1} corresponding to ν_4 PO$_4$ of apatite were observed (Figure 4C).[58,59] The double peaks at ∼1451 and 1418 cm^{-1} were

assigned to ν_3 CO$_3$, and the relatively weak peak at ∼874 cm^{-1} was assigned to ν_2 of B-substituted carbonate.[61,62] Importantly, the hydroxyl-deficient characteristic is based on the absence of sharp peaks at ∼3570 and 624 cm^{-1} (Figure 4C).[63] In region c, the position of ν_2 CO$_3$ at ∼878 cm^{-1} indicates that this is predominantly type A-substituted carbonated apatite.[64] Interestingly, in region c, in addition to ν_3 PO$_4$ peak at ∼1020 cm^{-1}, the carbonate peak around ∼1070 cm^{-1} also can be visualized.[65]

The amide I to ν_3 PO$_4$ ratios in regions a and c were 0.32 and 0.23, respectively, suggesting the presence of protein content. These data are consistent with our observations that Zn-rich organic substrates can act as scaffolds with various nuclei for minerals to precipitate, as demonstrated in Figure 2.

EDX characterization and principal component analysis (PCA) revealed the distribution of organic and inorganic phases. PCA analysis on the thick filamentous network revealed C, N, and O-rich organic regions (Figure 5A, PC 1). A strong sulfur signal also was identified in PC 2. Zn−S forms a critical biological partnership in creating the zinc finger motif in proteins.[66] In addition, sulfur-containing molecules such as metallothionines participate in response to inflammation[67] and could be potential sources for the observed sulfur signal. The primary minerals detected were associated with calcium and phosphorus elements in PC3, accompanied by smaller amounts of Na and Mg in PC4. Magnesium is a crucial micronutrient essential for the immune system[68,69] and can influence mineral precipitation kinetics.[70,71] The concurrent presence of P, O, Na, Mg, and Ca in PC4 suggests that sodium and magnesium phosphate salts may coexist alongside the predominant calcium phosphate precipitation. This observation was substantiated with PCA analyses on a highly mineralized area (Figure 5B) and a microbial colony encrusted with an inorganic shell (Figure 5C). PCA of multiple matrix stones further verified the clustering of Zn, C, S, and N in regions with higher zinc concentrations (red circle), while Ca, Na, P, and Mg clustered in areas with lower zinc concentrations (Figure 5D).

XRD characterizations revealed two distinct patterns in high zinc and high calcium regions (Figure 5E). The presence of apatite was identified in both regions. Notably, in the high zinc region, the XRD pattern demonstrated additional peaks (blue) on top of apatite peaks (red), suggesting the presence of whitlockite with the formula Ca$_9$(MgFe)(PO$_4$)$_6$PO$_3$OH. In addition, XRD lattice parameters indicated that the high zinc region exhibited a smaller unit cell volume, indicating the incorporation of Zn and the formation of a Zn apatite phase.[72]

■ CONCLUSIONS

In this study, by using a top-down approach, comprehensive correlative maps of elements, mineral phases, and molecular composition of matrix stones emphasizing their heterogeneous nature were presented. The outcomes of this study are based on the analysis of surgically extracted stones, with their initial formation unknown. However, details highlighted in this study from micro-to macro-scales provided insights into the temporal progression of the causative relationships and hypothesized renal biomineralization pathways.

We have expanded upon the conventional microbe-induced pathologic mineralization concept by emphasizing on the intricate host and microbe biological and biochemical interactions as upstream events that promote the biogenesis of an organic scaffold from the urine milieu. Failed attempts to

clear the scaffold with microbial colonies can antagonize the host immune response, furthering the growth of organic filamentous network. This host–microbe-derived scaffold, with an increased affinity for heterogeneous nucleation, is destined to undergo mineralization. If not removed from the host, it can subsequently form a clinically detectable stone. This "hidden effect" of the host immune response, as elusive as it may be, should not be overlooked. This unintended host–microbe interplay has a "double-edged sword" effect and significantly contributes to pathological biomineralization in the calyx of the human kidney.

■ ASSOCIATED CONTENT

Ⓢ Supporting Information

The Supporting Information is available free of charge at https://pubs.acs.org/doi/10.1021/acsnanoscienceau.2c00060.

> Patient care CT and photographs of matrix stones; SEM and TEM images of spherical bacterial colonies in matrix stone specimens; additional SEM images of matrix stone specimens; fluorescence microscopy images of CD63- and CD86-labeled matrix stone specimen sections, contrasted with control samples; proteomic studies and TEM images of matrix stone specimens revealing neutrophil extracellular trap formation; identification of genera of microbes within matrix stone specimens; images of PAS-stained matrix stone specimens; spatial map of calcium, zinc, and phosphorus elements obtained from XRF characterization of the matrix stone section; and FTIR spectra and polarized microscopy images of the matrix stone section (PDF)
>
> Pertinent clinical lab details (XLSX)
>
> Quantification of proteins in matrix stones (PDF)
>
> Functional enrichment analysis of matrix stone proteins. (PDF)
>
> Microbial proteins in matrix stones (PDF)

■ AUTHOR INFORMATION

Corresponding Author

Sunita P. Ho − *Department of Urology, School of Medicine and Department of Preventive and Restorative Dental Sciences, School of Dentistry, University of California San Francisco, San Francisco, California 94143, United States;* ⓘ orcid.org/0000-0001-9999-8226; Email: Sunita.Ho@ucsf.edu

Authors

Yushi Bai − *Department of Preventive and Restorative Dental Sciences, School of Dentistry, University of California San Francisco, San Francisco, California 94143, United States;* ⓘ orcid.org/0000-0003-1295-1615

Yongmei Wang − *Department of Preventive and Restorative Dental Sciences, School of Dentistry, University of California San Francisco, San Francisco, California 94143, United States*

Misun Kang − *Department of Preventive and Restorative Dental Sciences, School of Dentistry, University of California San Francisco, San Francisco, California 94143, United States*

Claire M. Gabe − *Department of Oral and Craniofacial Sciences, School of Dentistry, University of Pittsburgh, Pittsburgh, Pennsylvania 15213, United States*

Sudarshan Srirangapatanam − *Department of Preventive and Restorative Dental Sciences, School of Dentistry, University of California San Francisco, San Francisco, California 94143, United States; College of Medicine, University of Central Florida, Orlando, Florida 32827, United States*

Austin Edwards − *Biological Imaging Development Center, University of California San Francisco, San Francisco, California 94143, United States*

Marshall Stoller − *Department of Urology, School of Medicine, University of California San Francisco, San Francisco, California 94143, United States*

Stefan J. Green − *Department of Internal Medicine, Division of Infectious Diseases, Rush Medical College, Rush University, Chicago, Illinois 60612, United States*

Shaul Aloni − *The Molecular Foundry, Lawrence Berkeley National Laboratory, Berkeley, California 94720, United States*

Nobumichi Tamura − *Advanced Light Source, Lawrence Berkeley National Laboratory, Berkeley, California 94720, United States*

Elia Beniash − *Department of Oral and Craniofacial Sciences, School of Dentistry, University of Pittsburgh, Pittsburgh, Pennsylvania 15213, United States;* ⓘ orcid.org/0000-0001-9019-5160

Markus Hardt − *Center for Salivary Diagnostics, The Forsyth Institute, Cambridge, Massachusetts 02142, United States; Department of Developmental Biology, Harvard School of Dental Medicine, Boston, Massachusetts 02115, United States;* ⓘ orcid.org/0000-0002-2300-216X

Complete contact information is available at:
https://pubs.acs.org/10.1021/acsnanoscienceau.2c00060

Author Contributions

Y.B. and S.P.H. designed research; M.S. provided specimens and clinical insights; Y.B., Y.W., M.K., C.M.G., A.E., S.J.G., S.A., N.T., M.H., and S.P.H. performed research; Y.B., Y.W., M.K., C.M.G., S.S., A.E., S.J.G., S.A., N.T., E. B., M.H., and S.P.H. analyzed data; Y.B. and S.P.H. wrote the paper; and S.P.H. supervised the project. CRediT: **Yushi Bai** conceptualization (lead), data curation (lead), formal analysis (lead), investigation (lead), methodology (lead), validation (lead), visualization (lead), writing-original draft (lead), writing-review & editing (lead); **Yongmei Wang** data curation (supporting), methodology (supporting); **Misun Kang** data curation (supporting), formal analysis (supporting), methodology (supporting), visualization (supporting); **Claire M. Gabe** data curation (supporting), methodology (supporting); **Sudarshan Srirangapatanam** formal analysis (supporting), methodology (supporting), software (supporting); **Austin Edwards** formal analysis (supporting), software (supporting), visualization (supporting); **Marshall Stoller** conceptualization (supporting), funding acquisition (supporting), resources (lead), supervision (supporting), writing-original draft (supporting), writing-review & editing (supporting); **Stefan J Green** data curation (supporting), methodology (supporting); **Shaul Aloni** formal analysis (supporting), software (supporting); **Nobumichi Tamura** data curation (supporting), methodology (supporting); **Elia Beniash** data curation (supporting), methodology (supporting); **Markus Hardt** formal analysis (supporting), methodology (supporting), software (supporting), writing-original draft (supporting); **Sunita P Ho** conceptualization (lead), data curation (lead), formal analysis

■ REFERENCES

(1) Costerton, J. W.; Stewart, P. S.; Greenberg, E. P. Bacterial biofilms: a common cause of persistent infections. *Science* **1999**, *284*, 1318−1322.

(2) Vestby, L. K.; Grønseth, T.; Simm, R.; Nesse, L. L. Bacterial Biofilm and its Role in the Pathogenesis of Disease. *Antibiotics* **2020**, *9*, 59.

(3) Flores-Mireles, A. L.; Walker, J. N.; Caparon, M.; Hultgren, S. J. Urinary tract infections: epidemiology, mechanisms of infection and treatment options. *Nat. Rev. Microbiol.* **2015**, *13*, 269−284.

(4) Delcaru, C.; Alexandru, I.; Podgoreanu, P.; Grosu, M.; Stavropoulos, E.; Chifiriuc, M. C.; Lazar, V. Microbial Biofilms in Urinary Tract Infections and Prostatitis: Etiology, Pathogenicity, and Combating strategies. *Pathogens* **2016**, *5*, 65.

(5) Soto, S. M. Importance of Biofilms in Urinary Tract Infections: New Therapeutic Approaches. *Adv. Biol.* **2014**, *2014*, 1−13.

(6) Sharma, D.; Misba, L.; Khan, A. U. Antibiotics versus biofilm: an emerging battleground in microbial communities. *Antimicrob. Resist. Infect. Control* **2019**, *8*, 76.

(7) Domingue, J. C.; Drewes, J. L.; Merlo, C. A.; Housseau, F.; Sears, C. L. Host responses to mucosal biofilms in the lung and gut. *Mucosal Immunol.* **2020**, *13*, 413−422.

(8) Dongari-Bagtzoglou, A. Mucosal biofilms: challenges and future directions. *Expert Rev. Anti Infect. Ther.* **2008**, *6*, 141−144.

(9) Espinosa-Ortiz, E. J.; Eisner, B. H.; Lange, D.; Gerlach, R. Current insights into the mechanisms and management of infection stones. *Nat. Rev. Urol.* **2019**, *16*, 35−53.

(10) Wasfi, R.; Hamed, S. M.; Amer, M. A.; Fahmy, L. I. Proteus mirabilis Biofilm: Development and Therapeutic Strategies. *Front. Cell. Infect. Microbiol.* **2020**, *10*, 414.

(11) White, D. J. Dental calculus: recent insights into occurrence, formation, prevention, removal and oral health effects of supragingival and subgingival deposits. *Eur. J. Oral Sci.* **1997**, *105*, 508−522.

(12) Akcali, A.; Lang, N. P. Dental calculus: the calcified biofilm and its role in disease development. *Periodontol* **2018**, *76*, 109−115.

(13) Rao, A.; Berg, J. K.; Kellermeier, M.; Gebauer, D. Sweet on biomineralization: effects of carbohydrates on the early stages of calcium carbonate crystallization. *Eur. J. Mineral.* **2014**, *26*, 537−552.

(14) Qin, W.; Wang, C. Y.; Ma, Y. X.; Shen, M. J.; Li, J.; Jiao, K.; Tay, F. R.; Niu, L. N. Microbe-Mediated Extracellular and Intracellular Mineralization: Environmental, Industrial, and Biotechnological Applications. *Adv. Mater.* **2020**, *32*, No. e1907833.

(15) Gallagher, K.; Dupraz, C.; Braissant, O.; Decho, A.; Visscher, P.; Norman, R. Mineralization of sedimentary biofilms: Modern mechanistic insights. *Biofilm: Formation, Development and Properties, F, C*; Nova Science Publishers, 2010.

(16) Schwaderer, A. L.; Wolfe, A. J. The association between bacteria and urinary stones. *Ann. Transl. Med.* **2017**, *5*, 32.

(17) Khan, S. R. Heterogeneous nucleation of calcium oxalate crystals in mammalian urine. *Scanning Microsc.* **1995**, *9*, 597−614.

(18) Lahyani, M.; Rhannam, Y.; Slaoui, A.; Touzani, A.; Karmouni, T.; Elkhader, K.; Koutani, A.; Attya, A. I. Bilateral kidney matrix stones: a rare case. *Pan. Afr. Med. J.* **2016**, *25*, 102.

(19) Elawdy, M. M.; El-Halwagy, S.; Razek, Y. A.; Alsenani, A. R.; Almazroui, S. A Case of Pure Matrix Ureteral Stone: A rare type of urinary calculi that may be overlooked. *Sultan Qaboos Univ Med J.* **2019**, *18*, e557−e559.

(20) Koide, T.; Miyagawa, M.; Kinoshita, K. Matrix stones. *J. Urol.* **1977**, *117*, 786−787.

(21) Boyce, W. H.; King, J. S. Crystal-Matrix Interrelations in Calculi. *J. Urol.* **1959**, *81*, 351−365.

(22) Djomehri, S. I.; Candell, S.; Case, T.; Browning, A.; Marshall, G. W.; Yun, W.; Lau, S.; Webb, S.; Ho, S. P. Mineral density volume gradients in normal and diseased human tissues. *PLoS One* **2015**, *10*, No. e0121611.

(23) Wiśniewski, J. R.; Zougman, A.; Nagaraj, N.; Mann, M. Universal sample preparation method for proteome analysis. *Nat. Methods* **2009**, *6*, 359−362.

(24) Mi, H.; Ebert, D.; Muruganujan, A.; Mills, C.; Albou, L.-P.; Mushayamaha, T.; Thomas, P. D. PANTHER version 16: a revised family classification, tree-based classification tool, enhancer regions and extensive API. *Nucleic Acids Res.* **2021**, *49*, D394−D403.

(25) Perez-Riverol, Y.; Bai, J.; Bandla, C.; García-Seisdedos, D.; Hewapathirana, S.; Kamatchinathan, S.; Kundu, D. J.; Prakash, A.; Frericks-Zipper, A.; Eisenacher, M.; et al. The PRIDE database resources in 2022: a hub for mass spectrometry-based proteomics evidences. *Nucleic Acids Res.* **2022**, *50*, D543−D552.

(26) Naqib, A.; Poggi, S.; Wang, W.; Hyde, M.; Kunstman, K.; Green, S. J. Making and sequencing heavily multiplexed, high-throughput 16S ribosomal RNA gene amplicon libraries using a flexible, two-stage PCR protocol. *Gene Expression Analysis: Methods and Protocols*; Springer, 2018; pp 149−169.

(27) Jackson, M.; Engen, P. A.; Forsyth, C. B.; Shaikh, M.; Naqib, A.; Wilber, S.; Frausto, D. M.; Raeisi, S.; Green, S. J.; Bradaric, B. D.; et al. Intestinal Barrier Dysfunction in the Absence of Systemic Inflammation Fails to Exacerbate Motor Dysfunction and Brain Pathology in a Mouse Model of Parkinson's Disease. *Front. Neurol.* **2022**, *13*, 13.

(28) Callahan, B. J.; McMurdie, P. J.; Rosen, M. J.; Han, A. W.; Johnson, A. J. A.; Holmes, S. P. DADA2: High-resolution sample inference from Illumina amplicon data. *Nat. Methods* **2016**, *13*, 581−583.

(29) Estaki, M.; Jiang, L.; Bokulich, N. A.; McDonald, D.; González, A.; Kosciolek, T.; Martino, C.; Zhu, Q.; Birmingham, A.; Vázquez-Baeza, Y.; et al. QIIME 2 enables comprehensive end to end analysis of diverse microbiome data and comparative studies with publicly available data. *Curr. Protoc. Bioinf.* **2020**, *70*, No. e100.

(30) Davis, N. M.; Proctor, D. M.; Holmes, S. P.; Relman, D. A.; Callahan, B. J. Simple statistical identification and removal of contaminant sequences in marker-gene and metagenomics data. *Microbiome* **2018**, *6*, 226−14.

(31) Onyango, L. A.; Dunstan, R. H.; Gottfries, J.; von Eiff, C.; Roberts, T. K. Effect of Low Temperature on Growth and Ultra-Structure of Staphylococcus spp. *PLoS One* **2012**, *7*, No. e29031.

(32) Giesbrecht, P.; Kersten, T.; Maidhof, H.; Wecke, J. Staphylococcal cell wall: morphogenesis and fatal variations in the presence of penicillin. *Microbiol. Mol. Biol. Rev.* **1998**, *62*, 1371−1414.

(33) Andreu, Z.; Yáñez-Mó, M. Tetraspanins in Extracellular Vesicle Formation and Function. *Front. Immunol.* **2014**, *5*, 442.

(34) Thongboonkerd, V. Roles for Exosome in Various Kidney Diseases and Disorders. *Front. Pharmacol.* **2020**, *10*, 1655.

(35) Yu, M.; Yang, S.; Sun, H.; Xia, Q. CD63 Promotes Hemocyte-Mediated Phagocytosis in the Clam, Paphia undulata. *J. Immunol. Res.* **2016**, *2016*, 1−6.

(36) Pfistershammer, K.; Majdic, O.; Stöckl, J.; Zlabinger, G.; Kirchberger, S.; Steinberger, P.; Knapp, W. CD63 as an Activation-Linked T Cell Costimulatory Element. *J. Immunol.* **2004**, *173*, 6000−6008.

(37) Petersen, S. H.; Odintsova, E.; Haigh, T. A.; Rickinson, A. B.; Taylor, G. S.; Berditchevski, F. The role of tetraspanin CD63 in antigen presentation via MHC class II. *Eur. J. Immunol.* **2011**, *41*, 2556−2561.

(38) Subauste, C. S.; de Waal Malefyt, R.; Fuh, F. Role of CD80 (B7.1) and CD86 (B7.2) in the Immune Response to an Intracellular Pathogen. *J. Immunol.* **1998**, *160*, 1831−1840.

(39) Li, W.; Katz, B. P.; Spinola, S. M.; Morrison, R. P. Haemophilus ducreyi-Induced Interleukin-10 Promotes a Mixed M1 and M2 Activation Program in Human Macrophages. *Infect. Immun.* **2012**, *80*, 4426−4434.

(40) Zhou, Y.; Yoshida, S.; Kubo, Y.; Yoshimura, T.; Kobayashi, Y.; Nakama, T.; Yamaguchi, M.; Ishikawa, K.; Oshima, Y.; Ishibashi, T. Different distributions of M1 and M2 macrophages in a mouse model of laser-induced choroidal neovascularization. *Mol. Med. Rep.* **2017**, *15*, 3949−3956.

(41) Brinkmann, V.; Reichard, U.; Goosmann, C.; Fauler, B.; Uhlemann, Y.; Weiss, D. S.; Weinrauch, Y.; Zychlinsky, A. Neutrophil Extracellular Traps Kill Bacteria. *Science* **2004**, *303*, 1532−1535.

(42) Brinkmann, V.; Zychlinsky, A. Entering the neutrophil trap. *Nat. Rev. Immunol.* **2021**, *21*, 615.

(43) Fuchs, T. A.; Abed, U.; Goosmann, C.; Hurwitz, R.; Schulze, I.; Wahn, V.; Weinrauch, Y.; Brinkmann, V.; Zychlinsky, A. Novel cell death program leads to neutrophil extracellular traps. *J. Cell Biol.* **2007**, *176*, 231−241.

(44) Kanehisa, M.; Goto, S. KEGG: kyoto encyclopedia of genes and genomes. *Nucleic Acids Res.* **2000**, *28*, 27−30.

(45) Urban, C. F.; Ermert, D.; Schmid, M.; Abu-Abed, U.; Goosmann, C.; Nacken, W.; Brinkmann, V.; Jungblut, P. R.; Zychlinsky, A. Neutrophil extracellular traps contain calprotectin, a cytosolic protein complex involved in host defense against Candida albicans. *PLoS Pathog.* **2009**, *5*, No. e1000639.

(46) Bıçakçı, E.; Demirtaş, C. Ö.; Çelikel, Ç.; Haklar, G.; Duman, D. G. Myeloperoxidase and calprotectin; Any role as non-invasive markers for the prediction of ınflammation and fibrosis in non-alcoholic steatohepatitis? *Turk. J. Gastroenterol.* **2020**, *31*, 681−687.

(47) Davies, M. J.; Hawkins, C. L. The Role of Myeloperoxidase in Biomolecule Modification, Chronic Inflammation, and Disease. *Antioxid. Redox Signaling* **2020**, *32*, 957−981.

(48) Borregaard, N.; Sørensen, O. E.; Theilgaard-Mönch, K. Neutrophil granules: a library of innate immunity proteins. *Trends Immunol.* **2007**, *28*, 340−345.

(49) Li, T.; Zhang, Z.; Li, X.; Dong, G.; Zhang, M.; Xu, Z.; Yang, J. Neutrophil Extracellular Traps: Signaling Properties and Disease Relevance. *Mediat. Inflamm.* **2020**, *2020*, 1−14.

(50) Hansson, G. C. Role of mucus layers in gut infection and inflammation. *Curr. Opin. Microbiol.* **2012**, *15*, 57−62.

(51) Voynow, J. A.; Young, L. R.; Wang, Y.; Horger, T.; Rose, M. C.; Fischer, B. M. Neutrophil elastase increasesMUC5AC mRNA and protein expression in respiratory epithelial cells. *Am. J. Physiol. Lung Cell Mol. Physiol.* **1999**, *276*, L835−L843.

(52) Linden, S. K.; Sutton, P.; Karlsson, N. G.; Korolik, V.; McGuckin, M. A. Mucins in the mucosal barrier to infection. *Mucosal Immunol.* **2008**, *1*, 183−197.

(53) Musa, M. Immune mechanism: a 'double-edged sword. *Malays. J. Med. Sci.* **2013**, *20*, 61−67.

(54) Maywald, M.; Wessels, I.; Rink, L. Zinc Signals and Immunity. *Int. J. Mol. Sci.* **2017**, *18*, 2222.

(55) Hojyo, S.; Fukada, T. Roles of Zinc Signaling in the Immune System. *J. Immunol. Res.* **2016**, *2016*, 1−21.

(56) Kolaczkowska, E.; Kubes, P. Neutrophil recruitment and function in health and inflammation. *Nat. Rev. Immunol.* **2013**, *13*, 159−175.

(57) Poli, V.; Pui-Yan Ma, V.; Di Gioia, M.; Broggi, A.; Benamar, M.; Chen, Q.; Mazitschek, R.; Haggarty, S. J.; Chatila, T. A.; Karp, J. M.; et al. Zinc-dependent histone deacetylases drive neutrophil extracellular trap formation and potentiate local and systemic inflammation. *Iscience* **2021**, *24*, 103256.

(58) Boskey, A.; Pleshkocamacho, N. FT-IR imaging of native and tissue-engineered bone and cartilage. *Biomaterials* **2007**, *28*, 2465−2478.

(59) Gadaleta, S.; Paschalis, E.; Betts, F.; Mendelsohn, R.; Boskey, A. Fourier transform infrared spectroscopy of the solution-mediated conversion of amorphous calcium phosphate to hydroxyapatite: new correlations between X-ray diffraction and infrared data. *Calcif. Tissue Int.* **1996**, *58*, 9−16.

(60) Hong, T.; Yin, J.-Y.; Nie, S.-P.; Xie, M.-Y. Applications of infrared spectroscopy in polysaccharide structural analysis: Progress, challenge and perspective. *Food Chem.: X* **2021**, *12*, 100168.

(61) Madupalli, H.; Pavan, B.; Tecklenburg, M. M. Carbonate substitution in the mineral component of bone: Discriminating the structural changes, simultaneously imposed by carbonate in A and B sites of apatite. *J. Solid State Chem.* **2017**, *255*, 27−35.

(62) Sønju Clasen, A.; Ruyter, I. Quantitative determination of type A and type B carbonate in human deciduous and permanent enamel by means of Fourier transform infrared spectrometry. *Adv. Dent. Res.* **1997**, *11*, 523−527.

(63) Rehman, I.; Bonfield, W. Characterization of hydroxyapatite and carbonated apatite by photo acoustic FTIR spectroscopy. *J. Mater. Sci.: Mater. Med.* **1997**, *8*, 1−4.

(64) Madupalli, H.; Pavan, B.; Tecklenburg, M. M. J. Carbonate substitution in the mineral component of bone: Discriminating the structural changes, simultaneously imposed by carbonate in A and B sites of apatite. *J. Solid State Chem.* **2017**, *255*, 27−35.

(65) Xu, C.; Reed, R.; Gorski, J. P.; Wang, Y.; Walker, M. P. The distribution of carbonate in enamel and its correlation with structure and mechanical properties. *J. Mater. Sci.* **2012**, *47*, 8035−8043.

(66) Maret, W. Zinc and Sulfur: A Critical Biological Partnership. *Biochemistry* **2004**, *43*, 3301−3309.

(67) Grimble, R. F. The Effects of Sulfur Amino Acid Intake on Immune Function in Humans. *J. Nutr.* **2006**, *136*, 1660S−1665S.

(68) Galland, L. Magnesium and immune function: an overview. *Magnesium* **1988**, *7*, 290−299.

(69) Kubenam, K. S. The Role of Magnesium in Immunity. *J. Nutr. Immunol.* **1994**, *2*, 107−126.

(70) Sakaguchi, Y.; Hamano, T.; Isaka, Y. Effects of Magnesium on the Phosphate Toxicity in Chronic Kidney Disease: Time for Intervention Studies. *Nutrients* **2017**, *9*, 112.

(71) Zhang, J.; Tang, L.; Qi, H.; Zhao, Q.; Liu, Y.; Zhang, Y. Dual Function of Magnesium in Bone Biomineralization. *Adv. Healthcare Mater.* **2019**, *8*, 1901030.

(72) Procopio, A.; Malucelli, E.; Pacureanu, A.; Cappadone, C.; Farruggia, G.; Sargenti, A.; Castiglioni, S.; Altamura, D.; Sorrentino, A.; Giannini, C.; et al. Chemical fingerprint of Zn−hydroxyapatite in the early stages of osteogenic differentiation. *ACS Cent. Sci.* **2019**, *5*, 1449−1460.